

Article

Highly Effectual Photocatalytic Remediation of Tetracycline under the Broad Spectrum of Sunlight by Novel BiVO₄/Sb₂S₃ Nanocomposite

Shelly Singla^{1,2}, Pooja Devi^{1,*}  and Soumen Basu^{2,*} 

¹ Materials Science and Sensor Application, Central Scientific Instruments Organisation, Chandigarh 160030, India

² School of Chemistry and Biochemistry, Thapar Institute of Engineering and Technology, Patiala 147004, India

* Correspondence: poojaiitr@csio.res.in (P.D.); soumen.basu@thapar.edu (S.B.)

Abstract: Heterojunction photocatalysts (PC) with controllable compositions and in-built electric fields have attracted extensive research interest for their use in the remediation of environmental pollutants, owing to their supreme photocatalytic activity. Here, a simple hydrothermal route synthesizing different mole ratios of BiVO₄/Sb₂S₃ is reported as the PC. The inclusion of Sb₂S₃ with BiVO₄ in the BiVO₄/Sb₂S₃ composite possesses the ability to harvest a wide spectrum of solar light, an increased surface area, and an effective charge separation of the charge carriers. The efficacy of the synthesized catalyst was gauged by the photocatalytic abatement of a recalcitrant pollutant, tetracycline. The highest decomposition efficacy of 88.7% (rate constant 0.01557 min⁻¹) was achieved with 0.3 g/L of 1:3 BiVO₄:Sb₂S₃ photocatalyst for the tetracycline under sunlight illumination for 120 min. The catalyst was found stable for up to five cycles with a significant retention of its efficacy. The post-degradation characterizations revealed that the photocatalyst is stable due to the intactness of its crystalline planes, morphology, and surface area. Further, gas chromatography–mass spectrometry (GC–MS) was performed to study the decomposed products formed by the abatement of tetracycline. Moreover, chemical oxygen demand/ total organic carbon (COD/TOC) removals of 80.9% and 85.4%, respectively, were observed for the tetracycline standards, while for real TC pills, it was found to be 78.3% and 82.1%, respectively. This signifies that the photocatalyst has good surface catalytic properties in comparison to the existing expensive and time-consuming physicochemical approaches used in industry.

Keywords: BiVO₄/Sb₂S₃; photocatalytic decomposition; solar light; tetracycline



Citation: Singla, S.; Devi, P.; Basu, S. Highly Effectual Photocatalytic Remediation of Tetracycline under the Broad Spectrum of Sunlight by Novel BiVO₄/Sb₂S₃ Nanocomposite. *Catalysts* **2023**, *13*, 731. <https://doi.org/10.3390/catal13040731>

Academic Editors: Sekar Karthikeyan and Boopathy Ramasamy

Received: 4 March 2023

Revised: 6 April 2023

Accepted: 7 April 2023

Published: 12 April 2023



Copyright: © 2023 by the authors. Licensee MDPI, Basel, Switzerland. This article is an open access article distributed under the terms and conditions of the Creative Commons Attribution (CC BY) license (<https://creativecommons.org/licenses/by/4.0/>).

1. Introduction

Some of the most pressing global problems, such as environmental contamination and growing energy demands, have been greatly exacerbated by the relentless spread of industrialization [1,2]. Water contamination has recently become one of the major global environmental problems as a result of increasing industrialization and humans' excessive resource use [3]. According to reports, more than two billion people lack access to clean drinking water, and millions of people pass away each year from illnesses caused by contaminated water [4]. The discharge of pharmaceutical contaminants into environmental resources, such as sediment, surface water, soil, ground water, and even drinking water, poses a major threat to both freshwater ecosystems and humans, in addition to marine ones [5]. Antibiotics are not well-absorbed by living things and are eliminated as unmetabolized parent chemicals through urine and feces. One of the most significant pharmaceutical pollutants, tetracycline (TC), is used extensively in both veterinary and human medicine throughout the world to treat infections [6]. However, the presence of TC in the aquatic environment can result in genetic transfer, bacterial drug resistance, and pose a hazard to

human health as well as to aquatic organisms [7]. It is essential to take serious action to remove this detrimental organic contaminant from the water [8].

Several approaches, including microbiological elimination, physical absorption, electrochemical oxidation, advanced oxidation, electrolysis, and membrane separation, have been developed to remove and degrade TC efficiently [9]. The effectiveness of these methods is diminished by the production of secondary pollutants during the last stage of treatment, and an inevitable rise in pressure as well as temperature [10]. Moreover, TC is difficult to remove by conventional wastewater treatment techniques owing to its stable molecular structure and poor biodegradability [11]. Therefore, it is imperative to find an effective method for eliminating TC from aquatic environments.

Photocatalysis have drawn much interest because it is an environmentally friendly, inexpensive, non-toxic, and very effective method [12,13]. In addition, the photocatalytic decomposition method helps to eradicate the refractory organic pollutants of TC from water by completely changing them into water and carbon dioxide [14]. Developing an efficient visible-light-driven photocatalyst is essential for photocatalysis.

BiVO_4 (BV) has emerged as a promising option due to its greater chemical stability, low band gap of ~ 2.4 eV, non-toxicity, and ability to absorb an optimum amount of sunlight [15]. Additionally, the holes present in the valence band (VB) of BiVO_4 have a high oxidizing property that is advantageous for the decomposition of organic contaminants [16]. However, pure BiVO_4 has poor photocatalytic performance since it possesses a higher recombination rate of photogenerated charges [17,18]. The hybridization of BiVO_4 with other semiconductor photocatalysts has become a popular choice, as the heterojunction formation reduces recombination and prolongs the lifetime of photoinduced charges owing to its synergistic effect [19]. About 80.6%, 90.3%, and 86.7% degradation of phenol, norfloxacin, and ciprofloxacin was attained with $\text{BiVO}_4/\text{g-C}_3\text{N}_4/\text{carbon nanotubes}$, BiVO_4/LDH , and CuS/BiVO_4 , respectively, under the illumination of solar light for 120 min and visible light for 90 min [20–22].

Sb_2S_3 (SBS) is thought to be a potential photocatalyst because of its narrow band gap of ~ 1.84 eV, its ability to absorb solar light, its non-carcinogenicity, and its inexpensiveness [23]. Therefore, the hybridization of Sb_2S_3 with BiVO_4 tends to enhance the photocatalytic performance of the latter by reducing the reintegration rate of charge carriers. $\text{Sb}_2\text{S}_3/\text{rGO}$, $\text{Sb}_2\text{S}_3/\alpha\text{Ag}_2\text{WO}_4$ was synthesized and 89% of rhodamine B and 91.23% of methylene blue were degraded under solar light and visible light for 150 min and 120 min, respectively [24,25].

Several photocatalytic degradation experiments have been reported in the literature with pristine BiVO_4 and Sb_2S_3 [26]. Although $\text{BiVO}_4/\text{Sb}_2\text{S}_3$ composites have been previously synthesized [27], but the different mole ratios of $\text{BiVO}_4/\text{Sb}_2\text{S}_3$ composites have not yet been synthesized. In addition, the impact of different mole ratios on photodegradation experiments with the colorless pollutant under natural sunlight has not yet, to the author's knowledge, been reported. A comparison of the synthesized heterojunction photocatalyst with the commercial $\text{TiO}_2\text{-P25}$ under different light sources has not been conducted.

Here, different mole ratios of $\text{BiVO}_4/\text{Sb}_2\text{S}_3$ (BVSBS) nanocomposite have been prepared using the hydrothermal method. The performance of the fabricated photocatalyst was tested using the photocatalytic degradation of the noxious colorless pollutant, TC, under the irradiation of natural sunlight. Different experiments, including the concentration of the photocatalyst, kinetic studies, the impact of pH, reusability, and scavenger studies, were conducted. The impact of different light sources on the degradation efficacy of TC was compared. In addition, the superiority of the synthesized photocatalysts was tested by comparing the degradation efficacy with that of commercial $\text{TiO}_2\text{-P25}$. Gas chromatography–Mass spectrometry (GC–MS) was performed to analyze the decomposed products which were formed. Mineralization studies were also carried out. Lastly, the photocatalytic mechanism was proposed.

2. Results and Discussions

2.1. X-ray Photo Electron Study (XPS)

The elemental composition, binding energy of the core electrons, and oxidation state of the elements were examined using XPS analysis. The XPS can distinguish between the spin-orbit splitting of metal ions into two conceivable states, i.e., when they have different binding energies. The survey spectra of the as-prepared composite are presented in Figure 1a. The peaks specify that antimony, sulfur, oxygen, bismuth, and vanadium are the main elements in the 13BVSBS composite. The presence of C 1s may be accredited to the adventitious carbon of the instrument. The least-square Gaussian-fit model was used to deconvolute. In the core level spectra of Bi, V, and O, the presence of deconvoluted peaks at binding energies of 159.3 and 164.7 eV (Figure 1b), 516.9 and 524.6 eV (Figure 1c), and 530.1 eV (Figure 1d) can be ascribed to Bi 4f_{7/2} and 4f_{5/2}, V 2p_{3/2} and 2p_{1/2}, and O 1s attributes to the +3, +5, and −2 oxidation states of Bi, V, and O, respectively. This confirms the successful synthesis of BV in the composite [28–31]. As depicted in Figure 1e, the doublet peak centered at a binding energy of 529.8 and 539.2 eV corresponds to Sb 3d_{5/2} and 3d_{3/2}, respectively, and suggests the +3 oxidation state of Sb [32]. The doublet peak of S at a binding energy of 161.3 and 163.1 eV, related to S 2p_{1/2} and S 2p_{3/2} due to spin-orbit coupling, were credited to the −2 oxidation state as represented in Figure 1f [32].

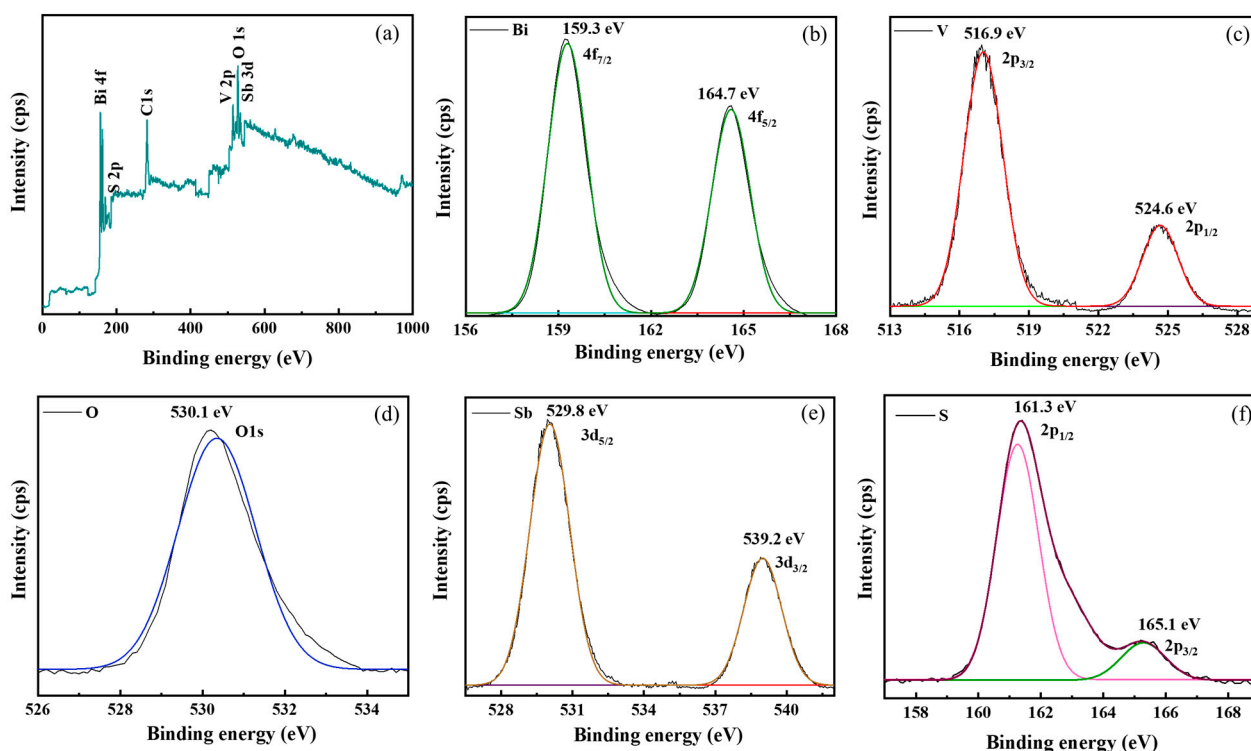


Figure 1. XPS spectrum of 13BVSBS photocatalyst: (a) survey spectra, (b) Bi 4f, (c) V 2p, (d) O 1s, (e) Sb 3d, and (f) S 2p.

2.2. X-ray Diffraction Analysis (XRD)

The crystallite phase, structural analyses, and purity of the photocatalysts were analyzed using XRD [33]. The XRD pattern of the prepared photocatalysts is provided in Figure 2a. The successful formation of hexagonal BiVO₄ was confirmed by the existence of peaks at 19.0° (011), 24.5° (102), 28.8° (112), 30.6° (004), 34.8° (200), 35.2° (020), 40.0° (211), 42.6° (015), 46.1° (123), 46.9° (204), 47.4° (024), 50.1° (220), 53.2° (301), and 58.3° (303), which matches the standard JCPDS card 83–1699 of BV. The diffraction peaks indexed at planes (110), (020), (120), (220), (130), (111), (230), (211), (221), (301), (311), (240), (231), (041), (141), (520), (440), (501), (531), and (132) corresponds to the 2θ value of 11.01°, 15.7°, 17.5°, 22.2°,

24.9°, 25.8°, 28.4°, 29.0°, 32.3°, 33.5°, 34.4°, 35.6°, 37.0°, 39.4°, 40.6°, 43.1°, 45.3°, 46.8°, 53.1°, and 54.2°, respectively, which matches well with the JCPDS card 00-006-0474, and confirms the efficacious formation of orthorhombic Sb_2S_3 . The synthesized BVSBS composites lack any impurity peaks. Further, little peak shifting was observed, indicating that the binary photocatalysts were of excellent purity and had a two-phase composition [34]. Additionally, the intensity of the peaks became stronger by increasing the concentration of SBS in the composite.

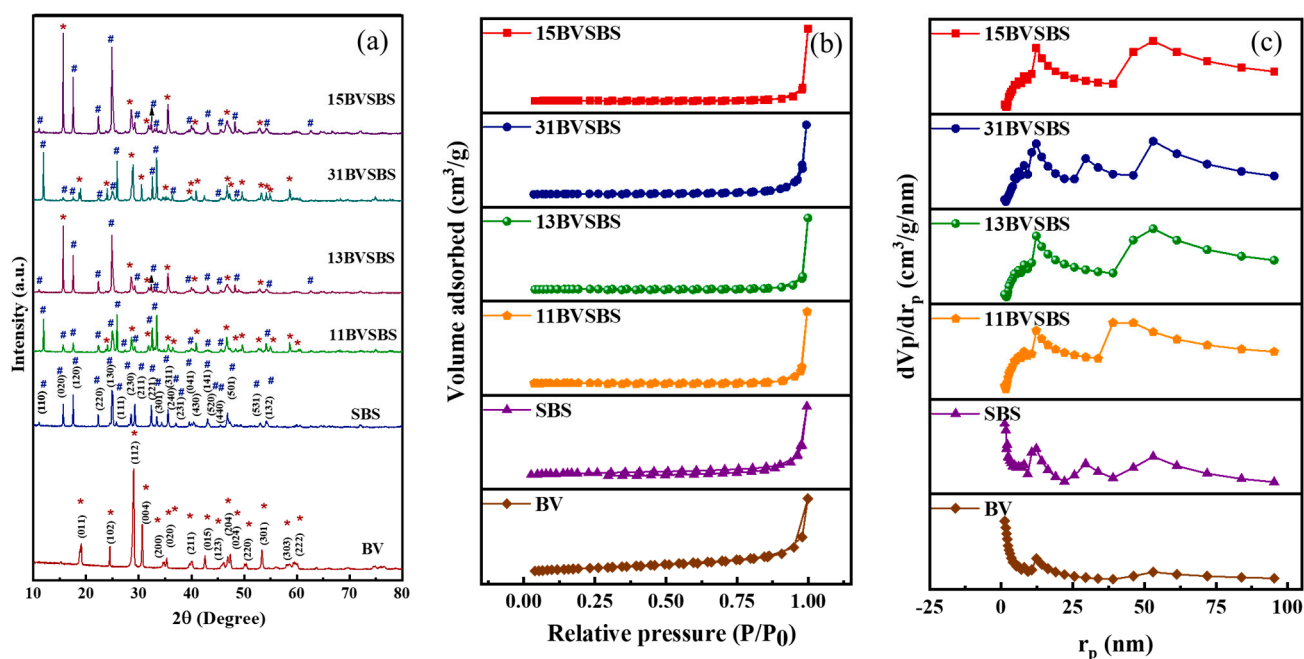


Figure 2. (a) XRD plot of the fabricated photocatalysts where * and # denote peaks of BV, and SBS, respectively, (b) BET surface area isotherm, and (c) BJH graph.

2.3. Photoluminescence Spectra (PL)

The migration, separation, and recombination of the photogenerated charge carriers can be examined using the PL spectra [35,36]. An efficacious photocatalyst should possess a low recombination rate, high carrier charge transport ability, and efficient separation of the charges [5,37]. The intensity of the PL signal is directly correlated to the recombination rate of the photogenerated excitons. The lower the PL emission intensity of a photocatalyst is, the less the recombination ability of the photoexcited carriers is, and thus the better the charge transfer efficiency is, which is advantageous for the photocatalytic performance of the photocatalyst [38]. An excitation wavelength of 325 nm was used to record the PL spectra. Pristine BV and SBS have the highest PL intensity, while the 13BVSBS and 15BVSBS photocatalysts have an analogous, and the lowest, PL intensity amongst all the photocatalysts, signifying the lowest recombination rate, good charge separation, and higher charge transport ability, as shown in Figure S1 (Supplementary Materials). This might be due to the formation of a heterojunction between BV and SBS, and the increased electron transport aids in decreasing the recombination rate of charges [39]. It was also analyzed that by increasing the amount of SBS in the composite, the PL intensity was considerably reduced.

2.4. Surface Area Analyses

The surface area of the photocatalysts is an important parameter in the field of photocatalysis. Nitrogen physisorption experiments were carried out to evaluate the surface area characteristics and pore size distribution of the prepared materials. The photocatalysts exhibit a type-IV N_2 adsorption curve, specifying that they possess a mesoporous

nature (Figure 2b,c). The pore size distribution was determined using the BJH plot. Table 1 summarizes the specific surface area results, and the mean pore diameter along with the pore volume calculated from the BJH plot. It was observed that the specific surface area and pore volume of the 13BVSBS and 15BVSBS hetero-composites are comparable and the highest among the prepared photocatalysts. The large surface area of the hetero-junction photocatalysts facilitates greater interfacial contact between both components for photoinduced charge migration and provides abundantly exposed surface-active sites to adsorb more pollutant, thereby improving photocatalytic activity [40]. The 13BVSBS and 15BVSBS catalyst composites exhibit the highest value among the various compositions of the synthesized photocatalyst.

Table 1. The surface area characteristics of the BVSBS photocatalysts.

Sample	Specific Surface Area (m ² /g)	Mean Pore Volume (cm ³ /g)	Mean Pore Diameter (nm)
BV	33	0.582	13.81
SBS	12	0.187	9.72
11BVSBS	38	0.242	11.10
13BVSBS	42	0.481	14.52
31BVSBS	39	0.372	11.70
15BVSBS	43	0.521	14.96

2.5. Absorption Studies

An optimum light absorption capability and a narrow band gap are the key features of a good photocatalyst. The absorption characteristics were measured using DRS to scrutinize the absorption range as well as the band gap of the synthesized photocatalysts. From Figure S2a, it can be seen that they display a significant visible light absorption capacity in the absorption range of 400–800 nm. A Tauc plot was used to calculate the band gap of the semiconductors according to Equation (1) [41].

$$(\alpha h\nu)^{1/2} = h\nu - E_g \quad (1)$$

where α = absorption coefficient, h = Planck's constant, ν = light's frequency, and E_g = intercepts of the tangents of the graphs depicting the band gap energy.

The Tauc plot was extrapolated to the photon energy ($h\nu$) axis to attain the E_g values [42]. Therefore, the band gaps of BV, SBS, 11BVSBS, 13BVSBS, 31BVSBS, and 15BVSBS were calculated to be 2.40, 1.80, 1.71, 1.51, 1.63, and 1.41 eV, respectively (Figure S2b). These results demonstrate that the 13BVSBS and 15BVSBS composites exhibit a narrow band gap, and the widest visible light absorption capacity among the synthesized catalysts.

2.6. Scanning Electron Microscopy (SEM) Analysis

The surface morphology of the BV, SBS, and 13BVSBS composites was examined using SEM at a differential magnification. According to the analysis, BV possesses a nano-rod-like structure, whereas SBS has a nano-sphere-like morphology (Figure 3a,b). The 13BVSBS composite features nano-spheres deposited onto a nano-rod-like structure, as shown in Figure 3c,d. Hence, the successful fabrication of the composite was validated due to the presence of both kinds of morphology. In addition, this type of morphology provides an ample number of active sites, therefore promoting more photocatalytic activity.

2.7. Energy Dispersive Spectroscopy (EDS) and Elemental Mapping

EDS was performed to gauge the elemental distribution, composition, and purity of the photocatalyst [43]. The EDS spectrum displays a significant signal from Bi, V, O, Sb, and S, all of which were effectively embedded inside the chosen regions of the 13BVSBS composite, as represented in Figure 4a. The lack of any other elemental peaks in the EDS spectrum suggests that the surface of the synthesized composite is devoid of any impurities, confirming its successful formation. The spatial distribution of Bi, V, O, Sb,

and S agrees well with the SEM of the composite, indicating that all the elements were uniformly dispersed (Figure 4b–f). These results demonstrate an excellent distribution of SBS onto BV, which is favorable for a heterojunction photocatalyst.

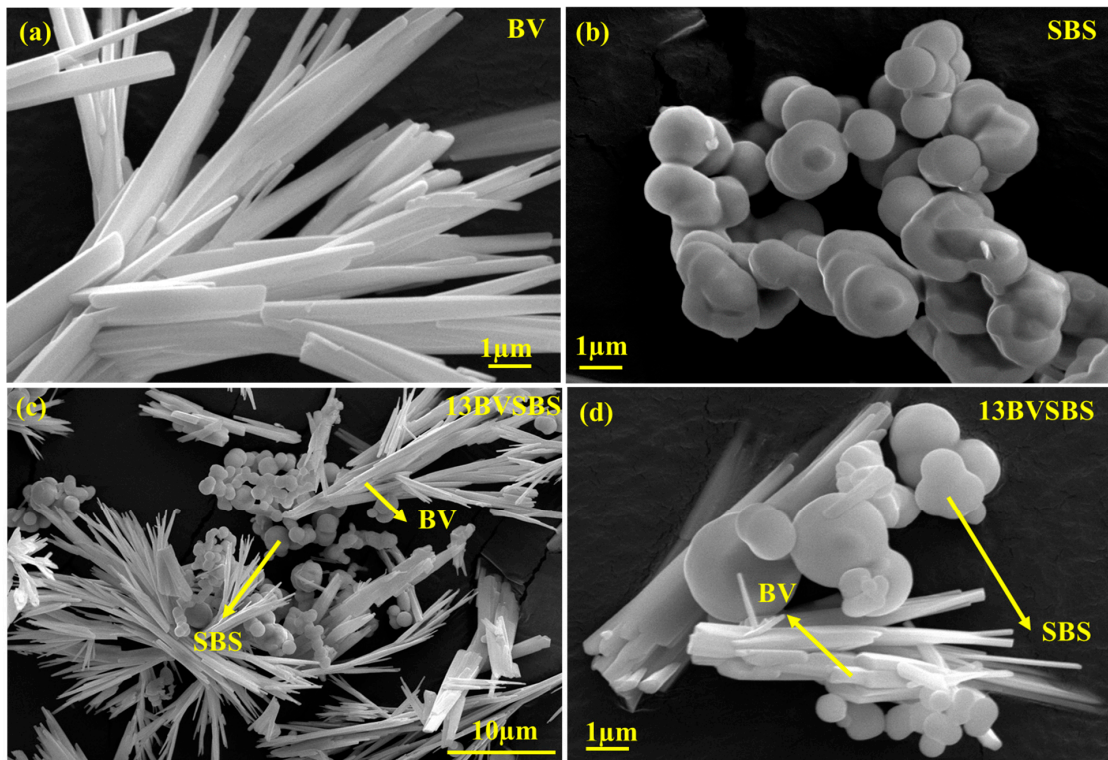


Figure 3. SEM images of (a) BV, (b) SBS, and (c,d) 13BVSBS photocatalyst with different magnification.

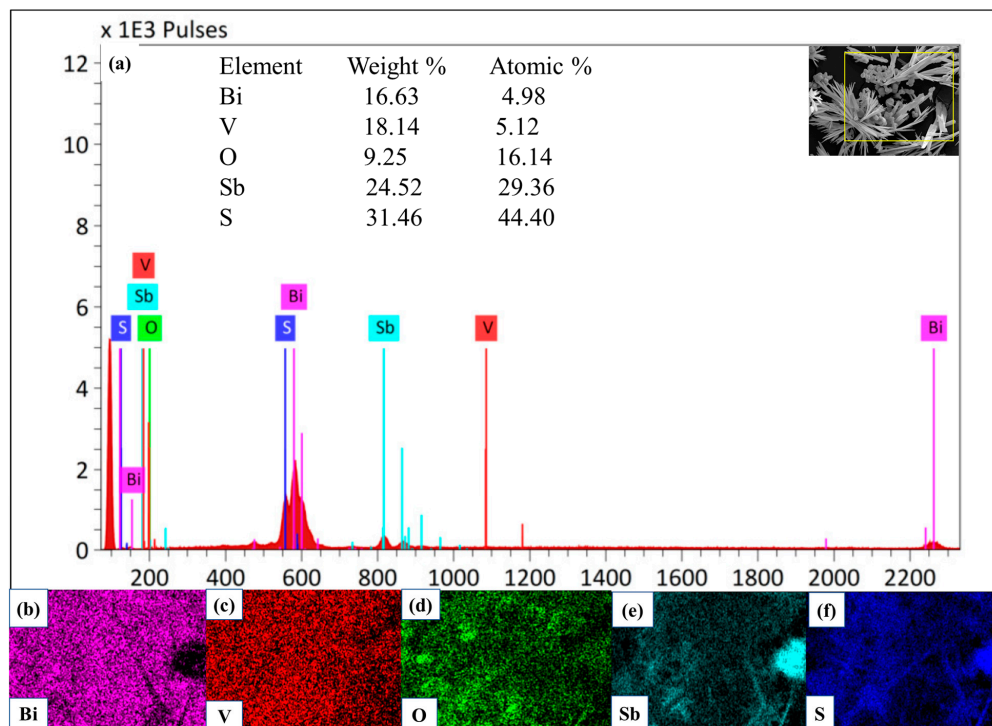


Figure 4. (a) EDS spectrum of the 13BVSBS photocatalyst with the corresponding SEM image and (b–f) elemental mapping of the 13BVSBS composite.

2.8. Photocatalytic Studies

A kinetic analysis of the photocatalytic deterioration of TC is represented in Figure 5a,b. The colorless pollutant, TC, was decomposed under sunlight to gauge the performance of the photocatalysts. When exposed to sunlight for 120 min, a 20 mL solution of TC decomposes at a low rate (8.9%) in the absence of a photocatalyst, as TC is a stable molecule. However, in the presence of 0.3 g/L of the 13BVSBS and 15BVSBS photocatalysts, up to 88.7% and 89.6% degradation of the TC was achieved, respectively. The photocatalytic activity of commercial TiO_2 -P25 powder was also compared to the synthesized catalysts and was found to exhibit a photoactivity of 47.0%. The lower performance of TiO_2 -P25 could be due to its wide band gap, thus rendering it responsive to UV light only. Therefore, the study revealed that the prepared photocatalysts exhibited superior photocatalytic activity over commercial TiO_2 -P25. The rate constant for the observed catalytic activity was determined using Equation (2), where k , C_0 , and C are the rate constant, initial concentration of the pollutant, and concentration at any time (t), respectively, and the outcomes are shown in Figure 5b.

$$\ln(C/C_0) = -kt \quad (2)$$

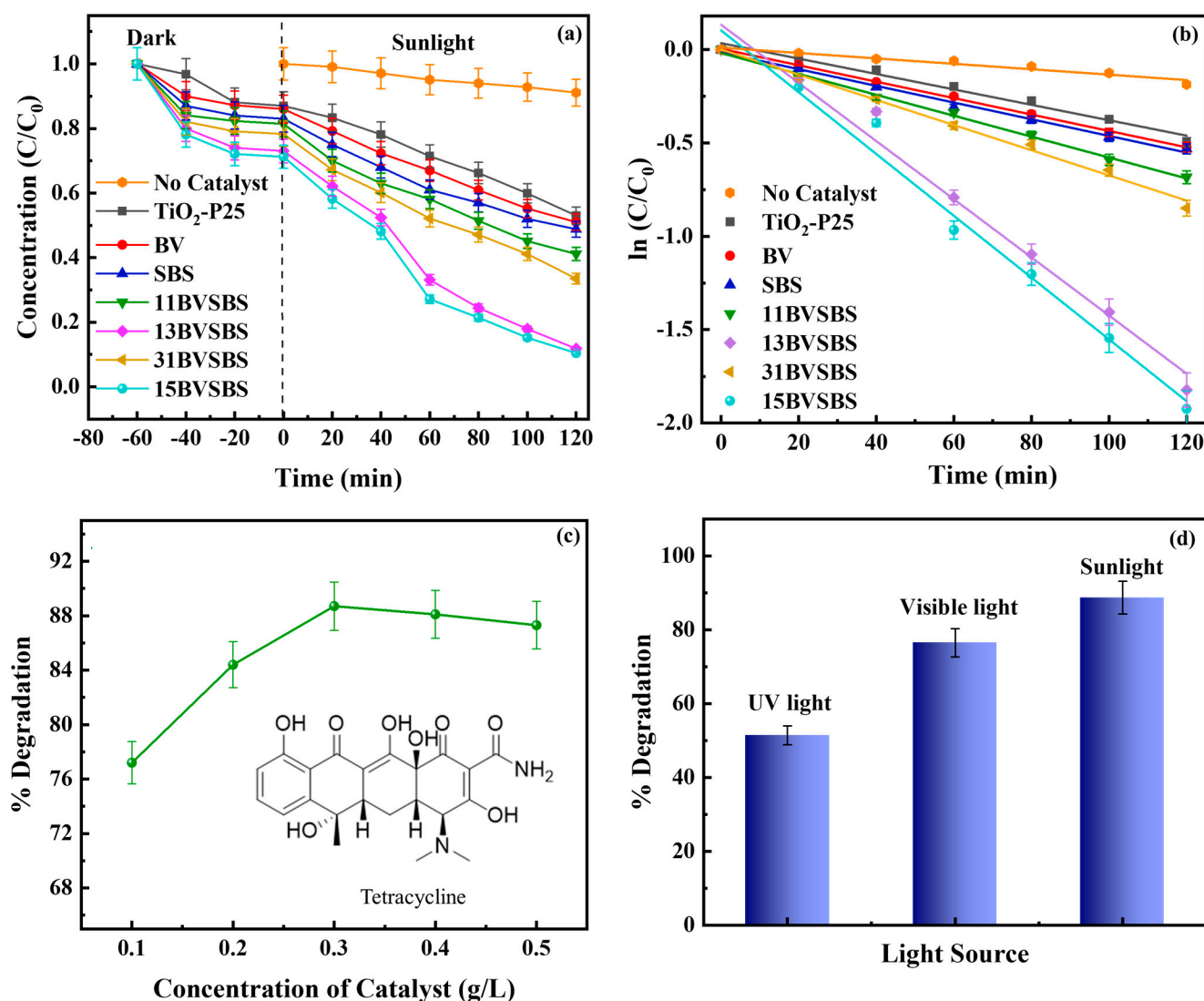


Figure 5. (a,b) Kinetic studies of the fabricated photocatalysts for the detoxification of TC, (c) concentration impact of the 13BVSBS photocatalyst, and (d) the effect of different light sources on the degradation efficiency of TC using the 13BVSBS photocatalyst.

It can be seen from Figure 5b that the reaction followed pseudo-first-order kinetics, i.e., the Langmuir–Hinshelwood kinetic model, owing to the good linear fitting of the lines ($R^2 > 98.5\%$) [44]. The 13BVSBS and 15BVSBS nanocomposites had the highest and analogous rate constants of 0.01557 min^{-1} and 0.01655 min^{-1} , respectively, among the prepared composites; meanwhile, the pristine BV and SBS exhibited rate constants of 0.00419 min^{-1} and 0.00447 min^{-1} , respectively. The rate constant of commercial $\text{TiO}_2\text{-P25}$ powder was also evaluated and found to be 0.00413 min^{-1} , which was the lowest among all the photocatalysts, revealing the superiority of the synthesized materials. Detailed photocatalytic studies were further carried out using 13BVSBS, since it was more efficient and cost-effective than 15BVSBS. The 15BVSBS exhibits similar activity but entails the use of a larger amount of SBS (the precursor salt of SBS is more expensive than BV). For the quantification of the degree of the synergistic effect of the composites, the synergy factor (R) was calculated using Equation (3).

$$R = \frac{\frac{k_{BV}}{k_{SBS}}}{k_{BV} + k_{SBS}} \quad (3)$$

Here, k , k_{BV}/k_{SBS} , k_{BV} , and k_{SBS} stand for the rate constant, the rate constant of hybrid BV and SBS, the bare BV, and SBS, respectively. The 13BVSBS had the highest R factor (1.75). This indicates that it had the highest efficiency amongst all the prepared materials owing to its higher synergistic effect on BV and SBS. The degradation efficacy, rate constant, and the value of the synergistic constant of the different photocatalysts are also tabularized in Table 2.

Table 2. Degradation efficacy, rate constant, and synergistic factor of the prepared photocatalysts.

Photocatalyst	Degradation (%)	Rate Constant (min^{-1})	Synergy (R) Factor
$\text{TiO}_2\text{-P25}$	47.0	$0.00413 \pm 2.57 \times 10^{-4}$	-
BV	49.1	$0.00419 \pm 5.84 \times 10^{-5}$	-
SBS	51.2	$0.00447 \pm 1.54 \times 10^{-4}$	-
11BVSBS	58.9	$0.00559 \pm 1.62 \times 10^{-4}$	0.64
13BVSBS	88.7	$0.01557 \pm 9.57 \times 10^{-4}$	1.75
31BVSBS	66.5	$0.00674 \pm 2.60 \times 10^{-4}$	0.77
15BVSBS	89.6	$0.01655 \pm 9.15 \times 10^{-4}$	1.91
No catalyst	8.90	$0.00079 \pm 1.46 \times 10^{-4}$	-

2.8.1. Impact of the Amount of Catalyst Loading

The ideal amount of catalyst used is one of the most important parameters affecting the degradation efficacy of the photocatalytic process. The use of the optimum amount of catalyst is crucial to avoid its excess use, which may promote the agglomeration of the particles, as well as to ensure the maximal absorption of photons for efficient photodecomposition [45]. As represented in Figure 5c, the degree of abatement of the TC was enhanced from 76.8% to 88.7% with an increase in the amount of the catalyst from 0.1 to 0.3 g/L, due to the increase in the sum of reaction sites. However, the decomposition efficacy declined slightly with a further increase in the amount of catalyst to 0.4 g/L. This is because when more of the catalyst is added to the solution, the turbidity of the solution increases, which disperses the light and reduces its impact on the solution [46]. In addition, the emergence of the active species is reduced as precipitation of the photocatalyst occurs. Therefore, for the subsequent experiments, a photocatalyst dose of 0.3 g/L was chosen as the best dosage based on the removal efficiency [47]. Thus, it can be inferred that even a little dose of the photocatalyst is enough for the photocatalytic abatement of TC under natural sunlight.

2.8.2. Effect of Light Sources

A similar experiment was conducted using different light sources (UV light and visible light) under optimum conditions to draw a comparison. From Figure 5d it can

be seen that TC degraded to 51.4% in UV light and 76.5% in visible light. However, the highest degradation rate of 88.7% was observed under natural sunlight with the 13BVSBS photocatalyst. Thus, sunlight is sufficient for the degradation of the pollutant using the synthesized photocatalysts.

2.8.3. Impact of pH

The pH is the most significant parameter in the photocatalytic decomposition process because it affects the capability of adsorption, the distribution of electric charges over the surface of the photocatalyst, and the degradation of the targeted organic contaminant by altering the surface charge properties of the photocatalyst, as well as varying the ionization state [48]. Thus, experiments were performed with varying pH values ranging from 2 to 12 to determine the influence of pH on the degrading efficacy of the TC. It was determined that with a rise in the pH of the solution, the degradation efficiency was first increased and then decreased, i.e., the composite's ability to degrade the TC was lower in an acidic environment than in an alkaline. A maximum degradation efficiency of 88.7% was observed at pH 7. The point of zero charge (pzc) of the photocatalyst was determined to be 5.8 (Figure 6a). TC is an amphoteric molecule and has three different acidic constants ($pK_{a1} = 3.30$, $pK_{a2} = 7.7$, and $pK_{a3} = 9.80$). At different pH values, the different ionizing functional groups of TC have different pKa values. TC exists as a cationic molecule (TCH_3^+ and TCH_2^+), because of the protonation of the dimethyl ammonium group, at $pH < 3.3$. It exists as an anionic species (TC_2^- and TCH^-), owing to the deprotonation of the tricarbon or diketone group of phenol, at $pH > 7.7$. However, it exists as an amphoteric form (TCH^\pm) when the pH ranges from 3.3 to 7.7, due to the abstraction of a proton from the diketone group of phenol [49]. The removal efficacy of TC using the 13BVSBS photocatalyst was decreased in acidic and alkaline environments due to the repulsive electrostatic forces emerging between the cationic and anionic forms of TC, and the surface of the positively and negatively charged photocatalyst, respectively. However, the electrostatic attraction between the negatively charged catalyst and the zwitterionic form of the pollutant enhanced the degradation efficiency of the pharmaceutical pollutant, TC. Hence, TC removal using the 13BVSBS composite was maximized at pH 7 and was higher in an alkaline than in an acidic environment, owing to the affinity of TC for the surface of the photocatalyst, as shown in Figure 6b.

2.8.4. Scavenger Studies

To scrutinize the role of the active radical species which are responsible for the photocatalytic elimination of TC, a trapping experiment was performed with commonly used quenchers. The chemical quenchers methanol, dimethyl sulfoxide (DMSO), and benzoquinone (BQ), each of 1 mM concentration, were used to investigate the role of holes (h^+), hydroxyl radicals ($\bullet OH$), and superoxide radicals ($O_2^{\bullet -}$), respectively, in the photocatalytic experiments [50]. In the absence of any trapping agent, a maximum degradation of the TC (88.7%) was observed. The inclusion of the above-mentioned scavengers in the reaction media efficiently quenched the photocatalytic decomposition of the TC. As shown in Figure 6c, the addition of DMSO significantly reduced the photocatalytic performance (32.4%) of the 13BVSBS composite, indicating that $\bullet OH$ is the major species responsible for pollutant decomposition. The degradation process was similarly affected by BQ (54.2%), albeit by a smaller amount, suggesting that $O_2^{\bullet -}$ plays a small but important role in the antibiotic elimination process. These findings demonstrate the susceptibility of $\bullet OH$ as the active species responsible for the photocatalytic elimination of TC in the presence of the 13BVSBS nanocomposite.

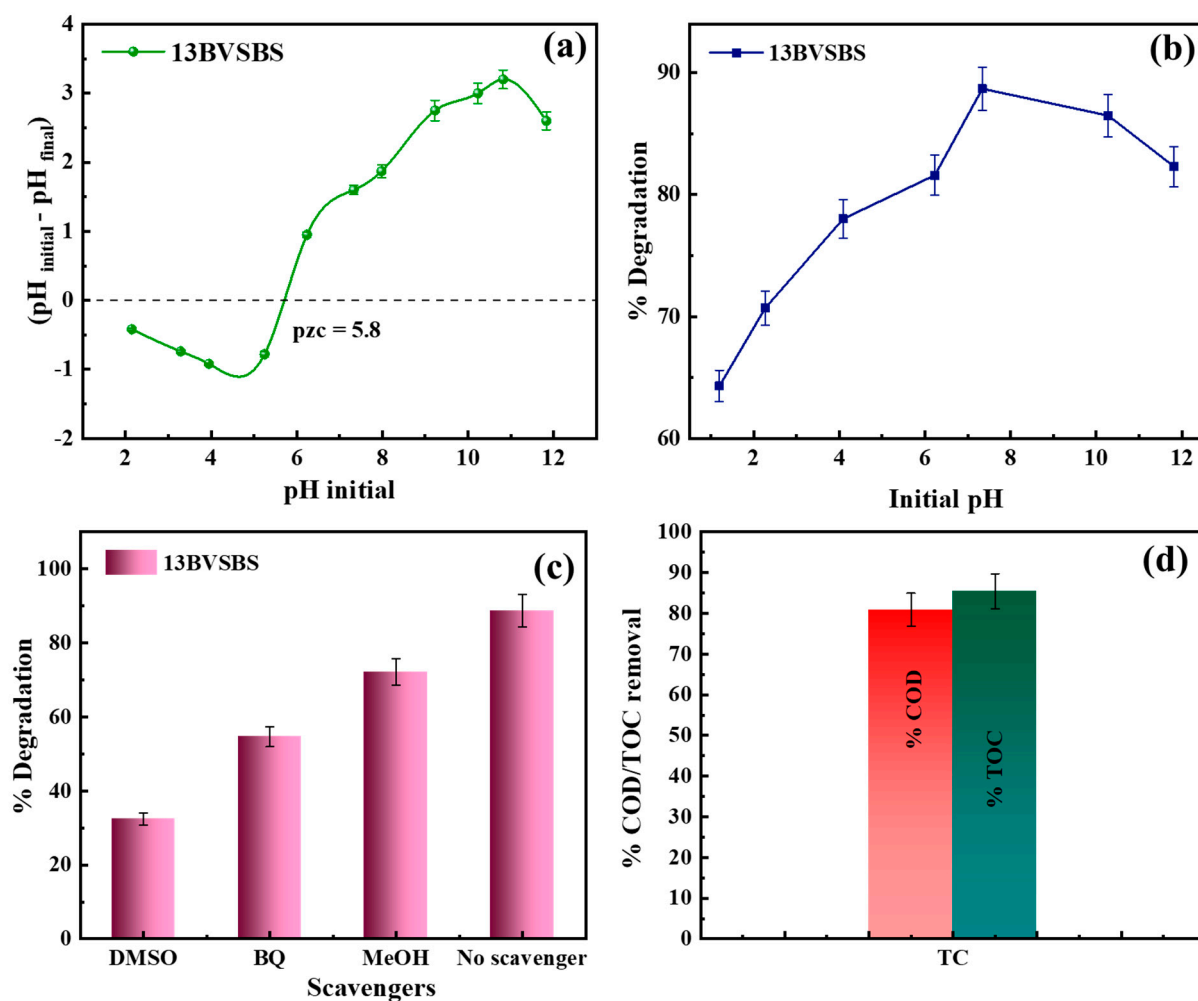


Figure 6. (a) pzc of the 13BVSBS nanocomposite, (b) impact of pH on the degradation efficiency of the 13BVSBS photocatalyst, (c) impact of different scavengers on the removal efficacy of the TC, and (d) COD and TOC analysis of a commercial sample of TC.

2.8.5. Mineralization Experiment

A total organic carbon (TOC) experiment was conducted to calculate the amount of TC mineralized by the 13BVSBS photocatalyst. The existence of a substantial amount of organic substances in the pollutant, TC, was initially demonstrated by a higher TOC and chemical oxygen demand (COD) levels. When the experiment was conducted utilizing the 13BVSBS photocatalyst under natural sunlight for 120 min, there was a 80.9% and 85.4% reduction in COD and TOC, respectively (Figure 6d). The % TOC removal was lower than the % degradation owing to the formation of sequential organic intermediates during the process before the complete breakdown of TC into carbon dioxide and other simpler products. In an aqueous solution, the degradation rate does not always imply extensive mineralization and the full destruction of organic compounds [23]. Due to ethical permission issues, experiments with real medical/pharmaceutical waste water cannot be performed. Therefore, the degradation efficacy of the 13BVSBS photocatalyst was tested by carrying out a COD and TOC analysis of a TC tablet (company name Abbott, Tetracycline capsules, I.P. Restecline 250, having a concentration of 250 mg) and was found to be 78.3% and 82.1%, respectively. This verifies that the photocatalyst has a good surface catalytic property in comparison to industries' existing expensive and time-consuming physicochemical approaches.

Photocatalytic materials must be stable and reusable in order to be used in real-world applications. Therefore, a reusability experiment was performed for five cycles to determine

the usefulness and stability of the photocatalyst for the photocatalytic degradation of TC [51]. 13BVSBS was chosen as the potential photocatalyst because it is easily separable, as the pollutant is physically adsorbed on its surface. The photocatalyst was centrifuged and rinsed with double distilled water before being dried at 50 °C for 10 h and reused for the next cycle. Following the fourth cycle, the decomposition of TC declined to 71.9%, in comparison to 88.7%, as depicted in Figure 7a. Loss of the photocatalyst may occur during the washing and the drying processes. Hence, the 13BVSBS nanocomposite is advantageous for use as a photocatalysis as it is reusable. In addition, the XRD pattern of the photocatalyst after carrying out reusability studies revealed no significant variations. Furthermore, the intensities and locations of all the diffraction peaks of BV and SBS remained intact after the reaction. No additional diffraction peaks, attributed to crystalline impurities formed after the recycling process, were observed (Figure 7b). In addition, a BET analysis performed after the recycling experiment confirmed that the photocatalyst had a specific surface area of 37 m²/g, a mean pore diameter of 11.22 nm, and a pore volume of 0.231 nm, respectively, as shown in Figure 7c,d. Although the surface area decreased, it was enough to proceed with the photocatalytic decomposition. As demonstrated in Figure 7e, the morphology of the 13BVSBS photocatalyst post-degradation experiment remained intact. Thus, it can be confirmed that the 13BVSBS photocatalyst had good recycling photocatalytic stability.

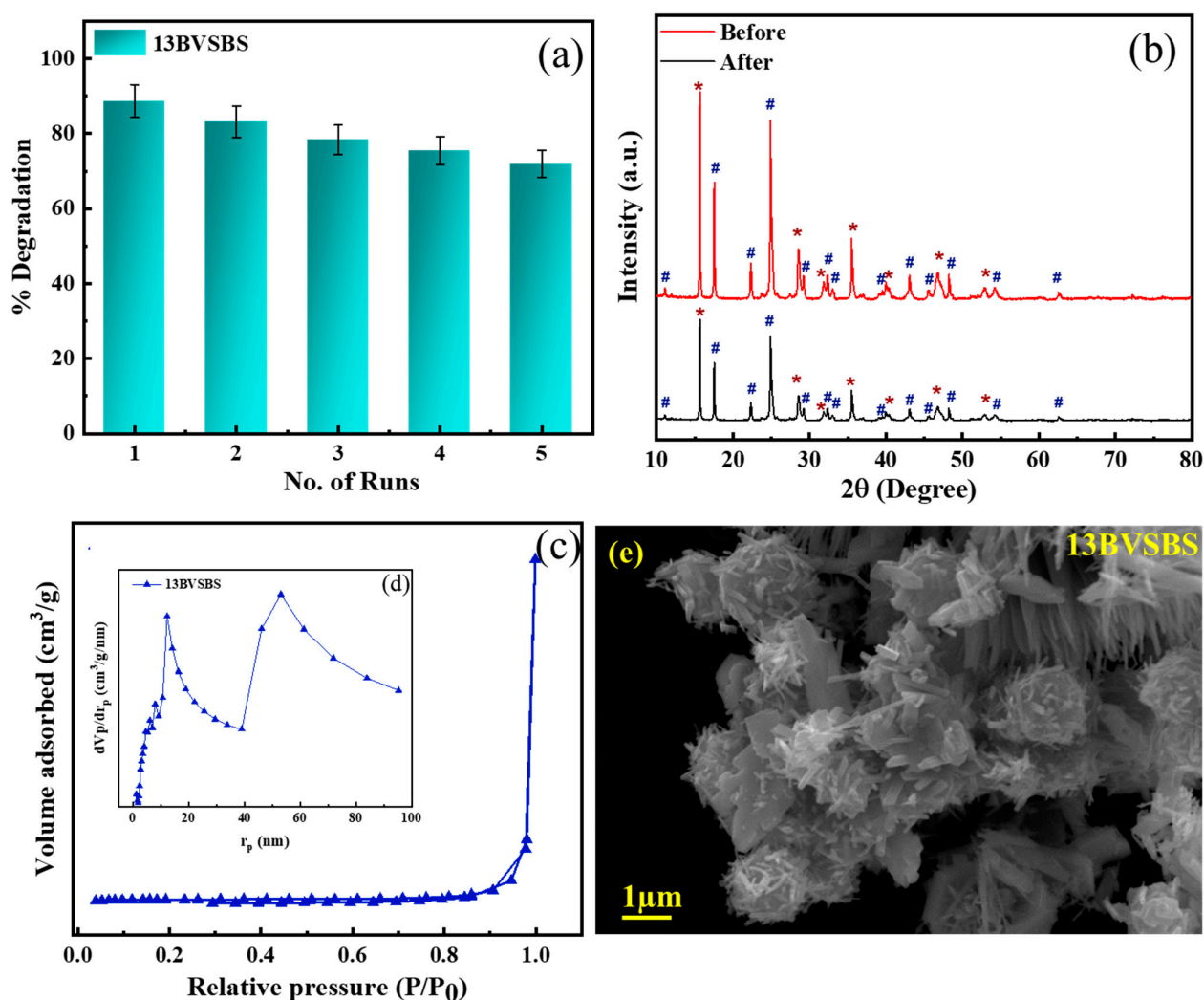


Figure 7. (a) The reusability graph, (b) XRD of 13BVSBS composite where * and # denote peaks of BV, and SBS, respectively, (c,d) BET with inset showing BJH graph, and (e) SEM image of the used catalyst's post degradation studies.

Table 3 summarizes a comparison study of different photocatalysts for the photocatalytic abatement of TC under different light sources. In comparison to the existing literature, the highest degradation efficacy can be achieved by using a small amount of the 13BVSBS photocatalyst under natural sunlight and optimum reaction conditions, such as pH and catalyst loading amount.

2.9. GC–MS Analysis

A GC–MS study was carried out to scrutinize the products and the intermediates formed in the photocatalytic breakdown process of TC. Figure S3a,b depicts the GC chromatogram and mass spectra, respectively. As represented in Figure 8, the photocatalytic decomposition follows three pathways. In the first route, deamination, ring opening, and demethylation of 4-(dimethylamino)-3,6,10,12,12a-pentahydroxy-6-methyl-1,11-dioxo-1,4,4a,5,5a,6,11,12a-octahydrotetracene-2-carboxamide resulted in the formation of 1-(2-(2-hydroxy-3-(propylamino) propoxy) phenyl)-3-phenylpropan-1-one. Further, 3,4-dimethylbenzaldehyde and 2,4-di-tert-butylphenol were formed by the addition of $O_2^{\bullet-}$ and $\bullet OH$ to 1-(2-(2-hydroxy-3-(propylamino) propoxy) phenyl)-3-phenylpropan-1-one. Oxidation of the intermediate species, the addition of $\bullet OH$, and the ring opening of 3,4-dimethylbenzaldehyde and 2,4-di-tert-butylphenol resulted in the formation of 2-ethylhexan-1-ol. Lastly, H_2O , CO_2 , and the simpler products were formed as a result of the abstraction of $\bullet OH$ and bond cleavage [52]. The second degradation route involved the formation of 5-hydroxy-2-phenyl-3a,4,7,7a-tetrahydro-1H-isoindole-1,3(2H)-dione by the abstraction of the electron from the organic moiety by the h^+ from 4-(dimethylamino)-3,6,10,12,12a-pentahydroxy-6-methyl-1,11-dioxo-1,4,4a,5,5a,6,11,12a-octahydrotetracene-2-carboxamide. The addition or substitution of $\bullet OH$ and ring cleavage led to the formation of 1,2,3,4-tetrahydronaphthalene. Furthermore, oxidation and ring cleavage resulted in the formation of o-cresol and ethane-1,2-diol, respectively [53]. In the third route, the indirect addition or substitution of $\bullet OH$ and the ring opening of 4-(dimethylamino)-3,6,10,12,12a-pentahydroxy-6-methyl-1,11-dioxo-1,4,4a,5,5a,6,11,12a-octahydrotetracene-2-carboxamide led to the production of two intermediate structures, 4-hydroxy-2,5-dimethylfuran-3(2H)-one and 3-(methoxycarbonyl)benzoic acid. After that, oxidation of these intermediate structures occurred and 3-hydroxybutanoic acid was formed. Finally, water and carbon dioxide were formed as products by fragmentation [54].

Table 3. Comparison of the different photocatalysts for the photocatalytic abatement of the colorless pollutant, TC.

Photocatalyst	Concentration of Pollutant	Reaction Time (min)	Light Source	Rate Constant k	Degradation Efficiency (%)	Ref.
BiVO ₄ /BiOI	10 ppm	60	Visible light	0.0133 min ⁻¹	69.57	[55]
BiVO ₄ /Bi ₂ SiO ₅	10 ppm	120	Visible light	0.0072 min ⁻¹	72.2	[56]
ZnInS ₄ /Sb ₂ S ₃	10 ppm	140	Visible light	0.009 min ⁻¹	85.36	[57]
Ag ₂ WO ₄ /Sb ₂ S ₃	10 ppm	180	Visible light	0.0041 min ⁻¹	53.06	[25]
BiOBr/g-C ₃ N ₄ /carbon nanofibers	-	120	Visible light	0.015 min ⁻¹	86.1	[9]
BVSBS	10 ppm	120	Sunlight	0.01557 min ⁻¹	88.7	Current work

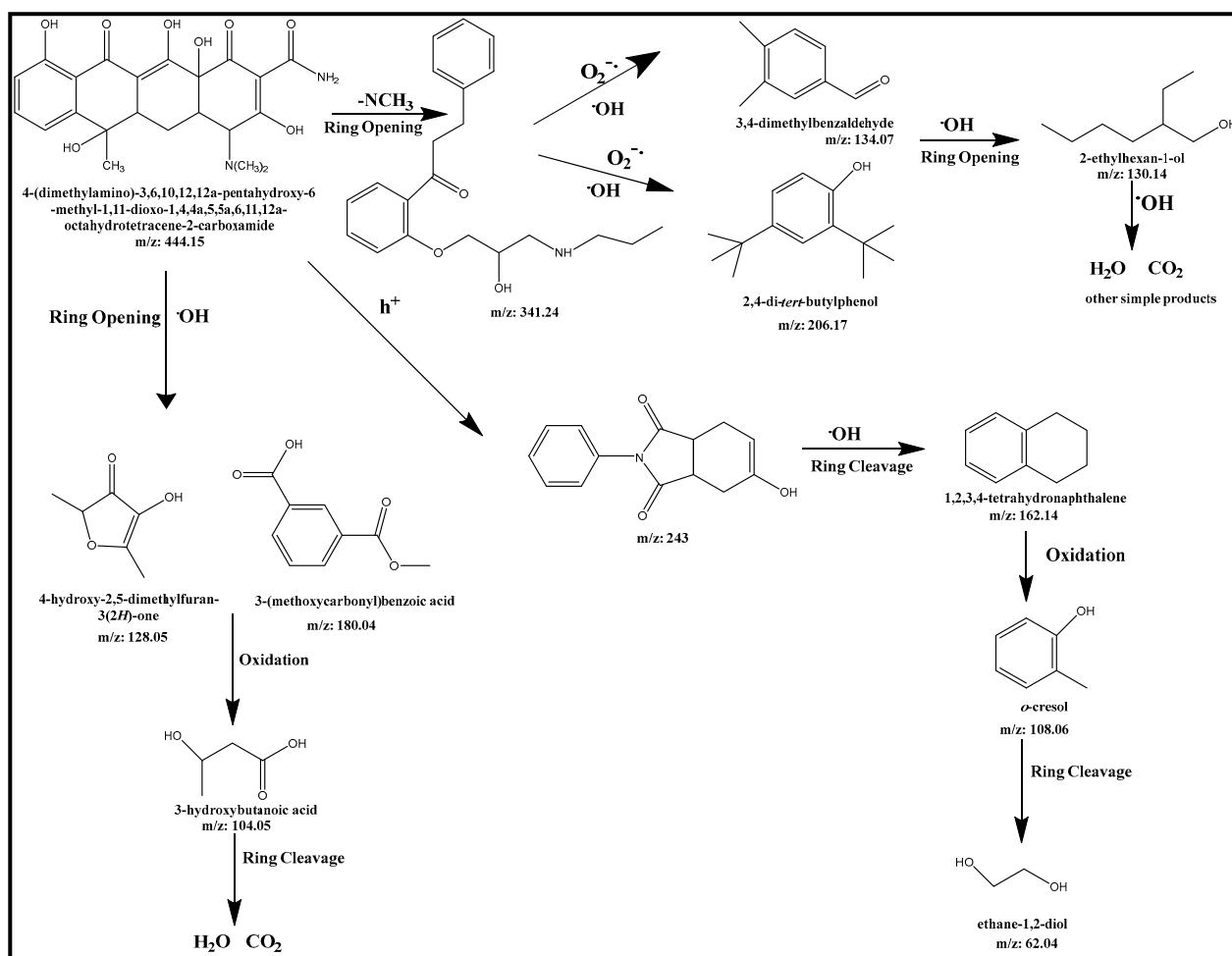


Figure 8. The deteriorated intermediate products formed by the photocatalytic remediation of TC by the 13BVSBS composite.

2.10. Photocatalytic Degradation Mechanism

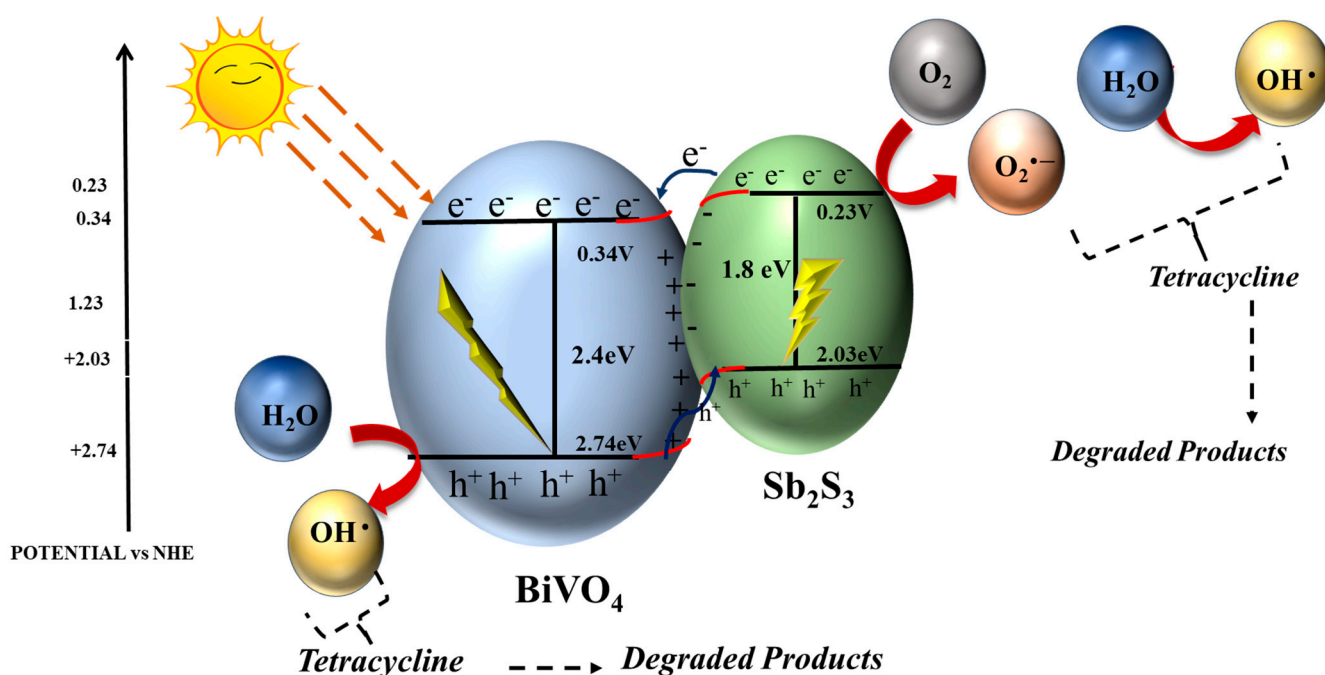
To understand the photocatalytic abatement of TC and the charge transport mechanism for photoactivity, the valence and the conduction band potential of the fabricated catalyst were gauged with Mulliken's Equations (4) and (5).

$$E_{VB} = \chi - E_e + 1/2E_g \quad (4)$$

$$E_{CB} = E_{VB} - E_g \quad (5)$$

Here, Mulliken's electronegativity, valence, and conduction band edge potential values are symbolized by χ , E_{VB} , and E_{CB} , respectively. The band gap edge value and the free electron energy on the hydrogen scale (4.5 eV) are signified by E_g and E_e , respectively. As a result, the E_{CB} potential values for BV and SBS were 0.34 and 0.23 eV, while the E_{VB} potential values were 2.74 and 2.03 eV, respectively [58,59]. Even after a longer period of illumination of the light, the accumulation of electrons is prevented due to the higher reintegration rate of the charge carriers of BV. During the illumination of light, electrons were transferred to the conduction band of both semiconductors as both are activated by sunlight. To avoid the reintegration rate of the photogenerated charge carriers of BV, electrons from the BV instinctively diffuse to the SBS when both semiconductors are in close proximity, forming an electron accumulation layer and depletion layer close to the interface of BV and SBS. An internal electric field that flows from BV to SBS is formed,

accelerating the migration of electrons from SBS to BV. In addition, the electrons in the conduction band of SBS and the holes in the valence band of BV are urged to reintegrate at the interface region by band bending. Thus, electrons present in the conduction band of SBS have the ability to react with $O_2^{\bullet-}$ and later have the potential to react with water to form OH^{\bullet} . This OH^{\bullet} radical can either directly oxidize and decompose the organic pollutants, or produce decomposed products from the oxidation of hazardous pollutants. In addition, the h^+ present in the valence band of BV has the ability to react with water to form OH^{\bullet} , which can further oxidize the detrimental pollutant to less toxic and simpler products. As depicted the Scheme 1, the photocatalysts follow a S-scheme heterojunction. Then the photocatalytic performance of the catalyst was compared to existing reports.



Scheme 1. The proposed photocatalytic mechanism.

3. Materials and Methods

Ethanol, sodium hydroxide pellets (NaOH), and acetic acid were purchased from Merck. Bismuth nitrate pentahydrate ($Bi(NO_3)_3 \cdot 5H_2O$), nitric acid (HNO_3), antimony chloride ($SbCl_3$), and ammonium metavanadate (NH_4VO_3) were procured from Spectrochem. Thioacetamide (CH_3CSNH_2) and Tartaric acid ($C_4H_6O_6$) were purchased from Loba Chemie. The pharmaceutical pollutant, TC, was bought from Sigma Aldrich. Deionized water ($18 M\Omega cm^{-1}$) was utilized to prepare the solutions. A TC tablet from Abbott (Tetracycline capsules, I.P. Restecline 250) with a concentration of 250 mg was purchased from a medical store.

3.1. Synthesis Protocol of $BiVO_4$

$BiVO_4$ was synthesized using an environmentally safe hydrothermal procedure. Typically, 5 mmol of $Bi(NO_3)_3 \cdot 5H_2O$ was dispersed in 10 mL HNO_3 (4 M) with continuous stirring. In another flask, NH_4VO_3 (5 mmol) was dissolved in 10 mL of NaOH (2 M) under vigorous stirring. About 0.25 g of $C_{18}H_{29}NaO_3S$ was dissolved in both of the prepared solutions. Afterward, both solutions were mixed together and a neutral pH was maintained by using NaOH (2 M). The resulting suspension was heated at 200 °C for 1.5 h in a Teflon-lined autoclave. A yellowish colored powder was centrifuged with distilled water and dried in an oven at 60 °C and was termed BV.

3.2. Synthesis Method of the BiVO₄/Sb₂S₃ Hybrid

The BiVO₄/Sb₂S₃ (BVSBS) couple with different mole ratios was fabricated using the hydrothermal synthesis method. Initially, BiVO₄ (0.0016 mol) was dissolved in 80 mL of distilled water to obtain a uniform solution. In this mixture, SbCl₃ (0.0016 mol), C₄H₆O₆ (0.010 mol), and CH₃CSNH₂ (0.0032 mol) were slowly added under vigorous stirring, followed by sonication for 1 h. The solution was heated at 180 °C for 8 h in a Teflon-lined stainless steel autoclave. After 3–4 washes with double distilled water and ethanol, the mixture was dried at 60 °C in a hot air oven. The resulting purplish powdery material was named 11BVSBS. The quantity of the chemicals needed to fabricate the various mole ratios (1:3, 3:1, and 1:5) were computed and named 13BVSBS, 31BVSBS, and 15BVSBS, respectively.

For comparison purposes, the purple-colored bare Sb₂S₃ was similarly synthesized without the addition of BiVO₄, and was labeled SBS.

3.3. Methods of Characterization

The characterization methods are described in Section S1.1 (Supplementary Materials).

3.4. Photocatalytic Elimination of TC

The decomposition of the recalcitrant antibiotic, TC, was performed under natural sunlight to assess the photocatalytic activity of the fabricated photocatalysts. About 6 mg of the photocatalyst was inoculated into 20 mL of 10 ppm of TC (0.3 g/L). Before the illumination, the solution was stirred at 900 rpm in the dark for 60 min to achieve an absorption–desorption equilibrium. Eventually, it was stirred under natural sunlight for 120 min to carry out degradation, by placing the test tubes vertically towards the sun. About 3 mL of solution was taken out at regular intervals and monitored through a UV-vis spectrophotometer after separating the catalyst using centrifugation. The experiments were conducted in July–August, and the sunlight intensity was 800–830 W/m² during these months as measured with the LICOR Pyranometer. The studies were carried out three times, and the plots are displayed with the error bars displaying a ~5% data source error. To monitor the degradation of the TC, the absorbance intensity of a UV-visible spectrophotometer was scrutinized at λ_{max} = 360 nm. The degradation efficacy is determined by using Equation (6).

$$\% \text{ Deg} = \{(Ab_0 - Ab_t)/Ab_0\} \times 100 = \{(C_0 - C_t)/C_0\} \times 100 \quad (6)$$

Here, % Deg, Ab₀, Ab_t is the degradation efficacy, initial absorbance, and absorbance at time t, respectively. C₀ and C_t is the initial concentration and concentration at time t, respectively.

GC–MS was performed to examine the degraded products produced after the photocatalytic elimination of the hazardous pharmaceutical pollutant, TC. The aqueous mixture was collected after the partitioning of the catalyst and the photocatalytic reaction. The residue was dissolved in the organic solvent, dichloromethane (DCM), and by drying at 38 °C in an oven, the solvent was vaporized. A Shimadzu GC–MS QP-2010 plus ultra-instrument with a split/split less injector was used. The conditions were as follows: split mode injector, ion source temperature = 220 °C, helium carrier gas (flow rate = 1.21 mL/min), injector temperature = 260 °C, and injection volume = 1 µL. The primary oven temperature was 100 °C for 2 min grip time; it was further augmented to 300 °C for 18 min hold time. MS spectra was captured at a range m/z = 40–650. COD and TOC analyses were used to assess the photocatalytic treatments for TC. Prior to the analysis, a 200 mL solution containing 60 mg of the 13BVSBS photocatalyst was illuminated with sunlight for 120 min. The COD was estimated via titration method, whereas the mineralization was computed using a TOC elimination. In order to compute the % COD and TOC eradication, Equations (7) and (8) were used.

$$\% \text{ COD} = \{(COD_i - COD_f)/COD_i\} \times 100 \quad (7)$$

$$\% \text{ TOC} = \{(TOC_i - TOC_f)/TOC_i\} \times 100 \quad (8)$$

Here, COD_i , COD_f , TOC_i , and TOC_f , designate the initial and final COD and TOC, respectively.

4. Conclusions

Various mole ratios of the novel heterojunction $BiVO_4/Sb_2S_3$ photocatalysts were fabricated using the environmentally friendly hydrothermal method. The characterization studies revealed that the binary composite possesses a high surface area and a low recombination rate, which is significant for the degradation of the detrimental pollutant. In addition, the composite had a narrow band gap allowing it to cover the broad range of solar light. The 13 BVSBS composite had a nano-sphere-like morphology deposited onto nano-rods. To gauge the photocatalytic performance of the fabricated photocatalysts, the photocatalytic remediation of the recalcitrant antibiotic, TC, was performed under natural sunlight. Different experiments, including the concentration of the photocatalyst, the pH effect of the detrimental pollutant, kinetic studies, effect of the light source, a scavenger study, and a reusability experiment were carried out. It was observed that with an increase in the concentration of SBS, the decomposition efficacy increased. The 13BVSBS and 15BVSBS exhibited the highest photocatalytic decomposition efficacies among the synthesized photocatalysts, of 88.7% and 89.6%, respectively. However, owing to its cost-effectiveness, 13BVSBS was considered to be the more efficacious photocatalyst. The decomposition efficacy of the synthesized nanocomposites was also compared to commercial TiO_2 -P25 to test the superiority of the prepared nanocomposites. The trapping studies confirmed that OH^\bullet radicals were the major scavenging agent in the decomposition experiment. The reusability experiment suggested that the synthesized photocatalysts are reusable and easily recoverable even after five cycles. The BET, SEM, and XRD post degradation experiments demonstrated that the surface area characteristics, morphology, and crystallinity of the material did not change after photocatalysis. GC–MS was carried out to validate the intermediates and the products formed during the breakdown of the TC. High % COD and % TOC values for the mineralization of TC confirmed that the synthesized composite is an excellent choice for the photocatalytic remediation of the detrimental antibiotic. Therefore, the BVSBS photocatalyst offers huge possibilities for the decomposition of detrimental pollutants.

Supplementary Materials: The following supporting information can be downloaded at: <https://www.mdpi.com/article/10.3390/catal13040731/s1>. Supplementary information comprises the characterization methods (Section S1.1), PL graph (Figure S1), absorbance plot (Figure S2a), Tauc plot (Figure S2b), gas chromatogram (Figure S3a), and mass spectra (Figure S3b) of the degraded products of TC using the 13BVSBS photocatalyst.

Author Contributions: S.S.: Conceptualization, formal analysis, methodology, and writing—original draft preparation. P.D.: Conceptualization, formal analysis, data curation, investigation, methodology, supervision, writing—review, and editing. S.B.: Conceptualization, formal analysis, data curation, investigation, methodology, supervision, writing—review, and editing. All authors have read and agreed to the published version of the manuscript.

Funding: This research received no external funding.

Data Availability Statement: The datasets generated during the current study are available from the corresponding authors upon reasonable request.

Acknowledgments: Shelly Singla is grateful to IIT, Delhi, for the XPS analysis. The authors are thankful to the Thapar Institute of Engineering and Technology for the XRD; JNU, Delhi, for the GC–MS analysis; and SAI Labs, TIET, Patiala, for the SEM and mineralization study.

Conflicts of Interest: The authors declare no conflict of interest.

References

1. Singla, S.; Sharma, S.; Basu, S. MoS₂/WO₃ Heterojunction with the Intensified Photocatalytic Performance for Decomposition of Organic Pollutants under the Broad Array of Solar Light. *J. Clean. Prod.* **2021**, *324*, 129290. [CrossRef]
2. Singla, S.; Sharma, S.; Basu, S.; Shetti, N.P.; Reddy, K.R. Graphene/Graphitic Carbon Nitride-Based Ternary Nanohybrids: Synthesis Methods, Properties, and Applications for Photocatalytic Hydrogen Production. *FlatChem* **2020**, *24*, 100200. [CrossRef]
3. Singla, S.; Sharma, S.; Basu, S.; Shetti, N.P.; Aminabhavi, T.M. Photocatalytic Water Splitting Hydrogen Production via Environmental Benign Carbon Based Nanomaterials. *Int. J. Hydrog. Energy* **2021**, *46*, 33696–33717. [CrossRef]
4. Pichel, N.; Vivar, M.; Fuentes, M. The Problem of Drinking Water Access: A Review of Disinfection Technologies with an Emphasis on Solar Treatment Methods. *Chemosphere* **2019**, *218*, 1014–1030. [CrossRef] [PubMed]
5. Singla, S.; Singh, P.; Basu, S.; Devi, P. BiVO₄/MoSe₂ Photocatalyst for the Photocatalytic Abatement of Tetracycline and Photoelectrocatalytic Water Splitting. *Mater. Chem. Phys.* **2023**, *295*, 127111. [CrossRef]
6. Yu, H.; Ge, D.; Liu, Y.; Lu, Y.; Wang, X.; Huo, M.; Qin, W. One-Pot Synthesis of BiOCl Microflowers Co-Modified with Mn and Oxygen Vacancies for Enhanced Photocatalytic Degradation of Tetracycline under Visible Light. *Sep. Purif. Technol.* **2020**, *251*, 117414. [CrossRef]
7. Fiaz, A.; Zhu, D.; Sun, J. Environmental Fate of Tetracycline Antibiotics: Degradation Pathway Mechanisms, Challenges, and Perspectives. *Environ. Sci. Eur.* **2021**, *33*, 64. [CrossRef]
8. Guo, J.; Jiang, L.; Liang, J.; Xu, W.; Yu, H.; Zhang, J.; Ye, S.; Xing, W.; Yuan, X. Photocatalytic Degradation of Tetracycline Antibiotics Using Delafossite Silver Ferrite-Based Z-Scheme Photocatalyst: Pathways and Mechanism Insight. *Chemosphere* **2021**, *270*, 128651. [CrossRef]
9. Shi, Z.; Zhang, Y.; Shen, X.; Duoerkun, G.; Zhu, B.; Zhang, L.; Li, M.; Chen, Z. Fabrication of G-C₃N₄/BiOBr Heterojunctions on Carbon Fibers as Weaveable Photocatalyst for Degrading Tetracycline Hydrochloride under Visible Light. *Chem. Eng. J.* **2020**, *386*, 124010. [CrossRef]
10. Kundu, A.; Sharma, S.; Basu, S. Modulated BiOCl Nanoplates with Porous G-C₃N₄ Nanosheets for Photocatalytic Degradation of Color/Colorless Pollutants in Natural Sunlight. *J. Phys. Chem. Solids* **2021**, *154*, 110064. [CrossRef]
11. Xiong, J.; Zeng, H.-Y.; Chen, C.-R.; Li, S.; Xu, S.; An, D.-S. Ag₃VO₄ Anchored ZnTi Hydroxalcite Microspheres with Rosette-like Structure for Tetracycline Degradation. *Appl. Clay Sci.* **2021**, *208*, 106118. [CrossRef]
12. Sharma, S.; Basu, S. Highly Reusable Visible Light Active Hierarchical Porous WO₃/SiO₂ Monolith in Centimeter Length Scale for Enhanced Photocatalytic Degradation of Toxic Pollutants. *Sep. Purif. Technol.* **2020**, *231*, 115916. [CrossRef]
13. Singla, S.; Shetti, N.P.; Basu, S.; Mondal, K.; Aminabhavi, T.M. Hydrogen Production Technologies—Membrane Based Separation, Storage and Challenges. *J. Environ. Manag.* **2022**, *302*, 113963. [CrossRef]
14. Sharma, S.; Basu, S. Visible-Light-Driven Efficient Photocatalytic Abatement of Recalcitrant Pollutants by Centimeter-Length MoO₃/SiO₂ Monoliths with Long Service Life. *Appl. Mater. Today* **2021**, *23*, 101033. [CrossRef]
15. Sadhasivam, S.; Anbarasan, N.; Gunasekaran, A.; Mukilan, M.; Jeganathan, K. Bi₂S₃ Entrenched BiVO₄/WO₃ Multidimensional Triadic Photoanode for Enhanced Photoelectrochemical Hydrogen Evolution Applications. *Int. J. Hydrog. Energy* **2022**, *47*, 14528–14541. [CrossRef]
16. Liu, L.; Hu, T.; Dai, K.; Zhang, J.; Liang, C. A Novel Step-Scheme BiVO₄/Ag₃VO₄ Photocatalyst for Enhanced Photocatalytic Degradation Activity under Visible Light Irradiation. *Chin. J. Catal.* **2020**, *42*, 46–55. [CrossRef]
17. Chen, F.; Yang, Q.; Sun, J.; Yao, F.; Wang, S.; Wang, Y.; Wang, X.; Li, X.; Niu, C.; Wang, D.; et al. Enhanced Photocatalytic Degradation of Tetracycline by AgI/BiVO₄ Heterojunction under Visible-Light Irradiation: Mineralization Efficiency and Mechanism. *ACS Appl. Mater. Interfaces* **2016**, *48*, 32887–32900. [CrossRef]
18. Wang, Y.; Ding, K.; Xu, R.; Yu, D.; Wang, W.; Gao, P.; Liu, B. Fabrication of BiVO₄/BiPO₄/GO Composite Photocatalytic Material for the Visible Light-Driven Degradation. *J. Clean. Prod.* **2020**, *247*, 119108. [CrossRef]
19. Samsudin, M.F.R.; Sufian, S. Hybrid 2D/3D g-C₃N₄/BiVO₄ Photocatalyst Decorated with RGO for Boosted Photoelectrocatalytic Hydrogen Production from Natural Lake Water and Photocatalytic Degradation of Antibiotics. *J. Mol. Liq.* **2020**, *314*, 113530. [CrossRef]
20. Samsudin, M.F.R.; Bacho, N.; Sufian, S.; Ng, Y.H. Photocatalytic Degradation of Phenol Wastewater over Z-Scheme g-C₃N₄/CNT/BiVO₄ Heterostructure Photocatalyst under Solar Light Irradiation. *J. Mol. Liq.* **2019**, *277*, 977–988. [CrossRef]
21. Zhang, L.; Meng, Y.; Dai, T.; Yao, Y.; Shen, H.; Xie, B.; Ni, Z.; Xia, S. Fabrication of a Coated BiVO₄@LDHs Z-Scheme Heterojunction and Photocatalytic Degradation of Norfloxacin. *Appl. Clay Sci.* **2022**, *219*, 106435. [CrossRef]
22. Lai, C.; Zhang, M.; Li, B.; Huang, D.; Zeng, G.; Qin, L.; Liu, X.; Yi, H.; Cheng, M.; Li, L.; et al. Fabrication of CuS/BiVO₄ (0 4 0) Binary Heterojunction Photocatalysts with Enhanced Photocatalytic Activity for Ciprofloxacin Degradation and Mechanism Insight. *Chem. Eng. J.* **2019**, *358*, 891–902. [CrossRef]
23. Sharma, S.; Basu, S. Fabrication of Centimeter-Sized Sb₂S₃/SiO₂ Monolithic Mimosa Pudica Nanoflowers for Remediation of Hazardous Pollutants from Industrial Wastewater. *J. Clean. Prod.* **2021**, *280*, 124525. [CrossRef]
24. Dashairya, L.; Sharma, S.; Rath, A.; Saha, P.; Basu, S. Solar-Light-Driven Photocatalysis by Sb₂S₃/Carbon Based Composites towards Degradation of Noxious Organic Pollutants. *Mater. Chem. Phys.* **2021**, *273*, 125120. [CrossRef]
25. Ayappan, C.; Jayaraman, V.; Palanivel, B.; Pandikumar, A.; Mani, A. Facile Preparation of Novel Sb₂S₃ Nanoparticles/Rod-like α-Ag₂WO₄ Heterojunction Photocatalysts: Continuous Modulation of Band Structure towards the Efficient Removal of Organic Contaminants. *Sep. Purif. Technol.* **2020**, *236*, 116302. [CrossRef]

26. Cao, F.; Liu, W.; Zhou, L.; Deng, R.; Song, S.; Wang, S.; Su, S.; Zhang, H. Well-Defined Sb_2S_3 Microspheres: High-Yield Synthesis, Characterization, Their Optical and Electrochemical Hydrogen Storage Properties. *Solid State Sci.* **2011**, *13*, 1226–1231. [[CrossRef](#)]
27. Lu, Y.; Wang, Z.; Su, J. Sb_2S_3 Surface Modification for Improved Photoelectrochemical Water Splitting Performance of BiVO_4 Photoanode. *J. Photonics Energy* **2021**, *11*, 016502. [[CrossRef](#)]
28. Liu, C.; Zhou, J.; Su, J.; Guo, L. Turning the Unwanted Surface Bismuth Enrichment to Favourable $\text{BiVO}_4/\text{BiOCl}$ Heterojunction for Enhanced Photoelectrochemical Performance. *Appl. Catal. B Environ.* **2019**, *241*, 506–513. [[CrossRef](#)]
29. Bai, Y.; Lu, J.; Bai, H.; Fang, Z.; Wang, F.; Liu, Y.; Sun, D.; Luo, B.; Fan, W.; Shi, W. Understanding the Key Role of Vanadium in P-Type BiVO_4 for Photoelectrochemical N_2 Fixation. *Chem. Eng. J.* **2021**, *414*, 128773. [[CrossRef](#)]
30. Tian, Y.; An, Y.; Wei, H.; Wei, C.; Tao, Y.; Li, Y.; Xi, B.; Xiong, S.; Feng, J.; Qian, Y. Micron-Sized Nanoporous Vanadium Pentoxide Arrays for High-Performance Gel Zinc-Ion Batteries and Potassium Batteries. *Chem. Mater.* **2020**, *32*, 4054–4064. [[CrossRef](#)]
31. Pang, Y.; Zhou, X.; Vovk, E.I.; Guan, C.; Li, S.; van Bavel, A.P.; Yang, Y. Understanding Lanthanum Oxide Surface Structure by DFT Simulation of Oxygen 1s Calibrated Binding Energy in XPS after in Situ Treatment. *Appl. Surf. Sci.* **2021**, *548*, 149214. [[CrossRef](#)]
32. Luo, W.; Ao, X.; Li, Z.; Lv, L.; Li, J.; Hong, G.; Wu, Q.H.; Wang, C. Imbedding Ultrafine Sb_2S_3 Nanoparticles in Mesoporous Carbon Sphere for High-Performance Lithium-Ion Battery. *Electrochim. Acta* **2018**, *290*, 185–192. [[CrossRef](#)]
33. Isari, A.A.; Mehregan, M.; Mehregan, S.; Hayati, F.; Rezaei Kalantary, R.; Kakavandi, B. Sono-Photocatalytic Degradation of Tetracycline and Pharmaceutical Wastewater Using WO_3/CNT Heterojunction Nanocomposite under US and Visible Light Irradiations: A Novel Hybrid System. *J. Hazard. Mater.* **2020**, *390*, 122050. [[CrossRef](#)]
34. Rajendran, S.; Khan, M.M.; Gracia, F.; Qin, J.; Gupta, V.K.; Arumainathan, S. Ce^{3+} -Ion-Induced Visible-Light Photocatalytic Degradation and Electrochemical Activity of ZnO/CeO_2 Nanocomposite. *Sci. Rep.* **2016**, *6*, 31641. [[CrossRef](#)]
35. Zhao, W.; Feng, Y.; Huang, H.; Zhou, P.; Li, J.; Zhang, L.; Dai, B.; Xu, J.; Zhu, F.; Sheng, N.; et al. A Novel Z-Scheme $\text{Ag}_3\text{VO}_4/\text{BiVO}_4$ Heterojunction Photocatalyst: Study on the Excellent Photocatalytic Performance and Photocatalytic Mechanism. *Appl. Catal. B Environ.* **2019**, *245*, 448–458. [[CrossRef](#)]
36. Singla, S.; Basu, S.; Devi, P. Solar Light Responsive 2D/2D $\text{BiVO}_4/\text{SnS}_2$ Nanocomposite for Photocatalytic Elimination of Recalcitrant Antibiotics and Photoelectrocatalytic Water Splitting with High Performance. *J. Ind. Eng. Chem.* **2023**, *118*, 119–131. [[CrossRef](#)]
37. Zhao, C.; Guo, J.; Yu, C.; Zhang, Z.; Sun, Z.; Piao, X. Fabrication of CNTs-Ag-TiO₂ Ternary Structure for Enhancing Visible Light Photocatalytic Degradation of Organic Dye Pollutant. *Mater. Chem. Phys.* **2020**, *248*, 122873. [[CrossRef](#)]
38. Zhang, R.; Cai, L.; Cai, Y.; Han, Q.; Li, Y.; Zhang, T.; Liu, Y.; Zeng, K.; Zhao, C.; Yu, J.; et al. Lamellar Insert SnS_2 Anchored on BiOBr for Enhanced Photocatalytic Degradation of Organic Pollutant under Visible-Light. *Colloids Surf. A Physicochem. Eng. Asp.* **2021**, *618*, 126444. [[CrossRef](#)]
39. Yang, L.; Wang, P.; Yin, J.; Wang, C.; Dong, G.; Wang, Y.; Ho, W. Engineering of Reduced Graphene Oxide on Nanosheet-g- C_3N_4 /Perylene Imide Heterojunction for Enhanced Photocatalytic Redox Performance. *Appl. Catal. B Environ.* **2019**, *250*, 42–51. [[CrossRef](#)]
40. Gnanasekaran, L.; Hemamalini, R.; Rajendran, S.; Qin, J.; Yola, M.L.; Atar, N.; Gracia, F. Nanosized Fe_3O_4 Incorporated on a TiO_2 Surface for the Enhanced Photocatalytic Degradation of Organic Pollutants. *J. Mol. Liq.* **2019**, *287*, 11097. [[CrossRef](#)]
41. Ali, W.; Ullah, H.; Zada, A.; Muhammad, W.; Ali, S.; Shaheen, S.; Alamgir, M.K.; Ansar, M.Z.; Khan, Z.U.; Bilal, H.; et al. Synthesis of TiO_2 Modified Self-Assembled Honeycomb ZnO/SnO_2 Nanocomposites for Exceptional Photocatalytic Degradation of 2,4-Dichlorophenol and Bisphenol A. *Sci. Total Environ.* **2020**, *746*, 141291. [[CrossRef](#)] [[PubMed](#)]
42. Méndez-Romero, U.A.; Pérez-García, S.A.; Xu, X.; Wang, E.; Licea-Jiménez, L. Functionalized Reduced Graphene Oxide with Tunable Band Gap and Good Solubility in Organic Solvents. *Carbon* **2019**, *146*, 491–502. [[CrossRef](#)]
43. Kamble, G.S.; Ling, Y.-C. Solvothermal Synthesis of Facet-Dependent BiVO_4 Photocatalyst with Enhanced Visible-Light-Driven Photocatalytic Degradation of Organic Pollutant: Assessment of Toxicity by Zebrafish Embryo. *Sci. Rep.* **2020**, *10*, 12993. [[CrossRef](#)] [[PubMed](#)]
44. Zamri, M.S.F.A.; Sapawe, N. Kinetic Study on Photocatalytic Degradation of Phenol Using Green Electrosynthesized TiO_2 Nanoparticles. *Mater. Today Proc.* **2019**, *19*, 1261–1266. [[CrossRef](#)]
45. Kamranifar, M.; Allahresani, A.; Naghizadeh, A. Synthesis and Characterizations of a Novel $\text{CoFe}_2\text{O}_4/\text{CuS}$ Magnetic Nanocomposite and Investigation of Its Efficiency for Photocatalytic Degradation of Penicillin G Antibiotic in Simulated Wastewater. *J. Hazard. Mater.* **2019**, *366*, 545–555. [[CrossRef](#)]
46. Monga, D.; Basu, S. Enhanced Photocatalytic Degradation of Industrial Dye by $\text{G-C}_3\text{N}_4/\text{TiO}_2$ Nanocomposite: Role of Shape of TiO_2 . *Adv. Powder Technol.* **2019**, *30*, 1089–1098. [[CrossRef](#)]
47. Wang, D.; Jia, F.; Wang, H.; Chen, F.; Fang, Y.; Dong, W.; Zeng, G.; Li, X.; Yang, Q.; Yuan, X. Simultaneously Efficient Adsorption and Photocatalytic Degradation of Tetracycline by Fe-Based MOFs. *J. Colloid Interface Sci.* **2018**, *519*, 273–284. [[CrossRef](#)]
48. Nasseh, N.; Hossein Panahi, A.; Esmati, M.; Daglioglu, N.; Asadi, A.; Rajati, H.; Khodadoost, F. Enhanced Photocatalytic Degradation of Tetracycline from Aqueous Solution by a Novel Magnetically Separable $\text{FeNi}_3/\text{SiO}_2/\text{ZnO}$ Nano-Composite under Simulated Sunlight: Efficiency, Stability, and Kinetic Studies. *J. Mol. Liq.* **2020**, *301*, 112434. [[CrossRef](#)]
49. Wang, X.; Jia, J.; Wang, Y. Combination of Photocatalysis with Hydrodynamic Cavitation for Degradation of Tetracycline. *Chem. Eng. J.* **2017**, *315*, 272–284. [[CrossRef](#)]

50. Gupta, D.; Chauhan, R.; Kumar, N.; Singh, V.; Srivastava, V.C.; Mohanty, P.; Mandal, T.K. Enhancing Photocatalytic Degradation of Quinoline by ZnO:TiO₂ Mixed Oxide: Optimization of Operating Parameters and Mechanistic Study. *J. Environ. Manag.* **2020**, *258*, 110032. [[CrossRef](#)]
51. Wang, X.; Jiang, L.; Li, K.; Wang, J.; Fang, D.; Zhang, Y.; Tian, D.; Zhang, Z.; Dionysiou, D.D. Fabrication of Novel Z-Scheme SrTiO₃/MnFe₂O₄ System with Double-Response Activity for Simultaneous Microwave-Induced and Photocatalytic Degradation of Tetracycline and Mechanism Insight. *Chem. Eng. J.* **2020**, *400*, 125981. [[CrossRef](#)]
52. Guo, P.; Zhao, F.; Hu, X. Boron- and Europium-Co-Doped g-C₃N₄ Nanosheets: Enhanced Photocatalytic Activity and Reaction Mechanism for Tetracycline Degradation. *Ceram. Int.* **2021**, *47*, 16256–16268. [[CrossRef](#)]
53. Pan, Y.; Hu, X.; Bao, M.; Li, F.; Li, Y.; Lu, J. Fabrication of MIL-Fe (53)/Modified g-C₃N₄ Photocatalyst Synergy H₂O₂ for Degradation of Tetracycline. *Sep. Purif. Technol.* **2021**, *279*, 119661. [[CrossRef](#)]
54. Xu, J.; Zhang, X.; Sun, C.; Wan, J.; He, H.; Wang, F.; Dai, Y.; Yang, S.; Lin, Y.; Zhan, X. Insights into Removal of Tetracycline by Persulfate Activation with Peanut Shell Biochar Coupled with Amorphous Cu-Doped FeOOH Composite in Aqueous Solution. *Environ. Sci. Pollut. Res.* **2019**, *26*, 2820–2834. [[CrossRef](#)]
55. Chen, Y.; Liu, Y.; Xie, X.; Li, C.; Si, Y.; Zhang, M.; Yan, Q. Synthesis Flower-like BiVO₄/BiOI Core/Shell Heterostructure Photocatalyst for Tetracycline Degradation under Visible-Light Irradiation. *J. Mater. Sci. Mater. Electron.* **2019**, *30*, 9311–9321. [[CrossRef](#)]
56. Wang, Z.-H.; Jia, Y.-N.; Wu, X.-F.; Song, M.-C.; Ma, X.-Y.; Wang, H.; Zhang, X.-F. Preparation and Characterization of Bi₂SiO₅/BiVO₄ n-n Iso-type Heterojunction Composites as a Visible-Light-Induced Photocatalyst for Tetracycline and Levofloxacin Degradation. *J. Mater. Sci. Mater. Electron.* **2023**, *34*, 433. [[CrossRef](#)]
57. Xiao, Y.; Wang, H.; Jiang, Y.; Zhang, W.; Zhang, J.; Wu, X.; Liu, Z.; Deng, W. Hierarchical Sb₂S₃/ZnIn₂S₄ Core-Shell Heterostructure for Highly Efficient Photocatalytic Hydrogen Production and Pollutant Degradation. *J. Colloid Interface Sci.* **2022**, *623*, 109–123. [[CrossRef](#)]
58. Zhang, J.; Deng, M.; Ren, F.; Wu, Y.; Wang, Y. Effects of Mo/W Codoping on the Visible-Light Photocatalytic Activity of Monoclinic BiVO₄ within the GGA + U Framework. *RSC Adv.* **2016**, *6*, 12290–12297. [[CrossRef](#)]
59. Yang, H.; Li, M.; Fu, L.; Tang, A.; Mann, S. Controlled Assembly of Sb₂S₃ Nanoparticles on Silica/Polymer Nanotubes: Insights into the Nature of Hybrid Interfaces. *Sci. Rep.* **2013**, *3*, 1336. [[CrossRef](#)]

Disclaimer/Publisher's Note: The statements, opinions and data contained in all publications are solely those of the individual author(s) and contributor(s) and not of MDPI and/or the editor(s). MDPI and/or the editor(s) disclaim responsibility for any injury to people or property resulting from any ideas, methods, instructions or products referred to in the content.